Electromagnetically Induced Transparency and Wideband Wavelength Conversion in Silicon Nitride Microdisk Optomechanical Resonators

Yuxiang Liu,[1,2] Marcelo Davanço,[1,3] Vladimir Aksyuk,[1] and Kartik Srinivasan[1,*]

[1]Center for Nanoscale Science and Technology, National Institute of Standards and Technology, Gaithersburg, Maryland 20899, USA
[2]Institute for Research in Electronics and Applied Physics, University of Maryland, College Park, Maryland 20742, USA
[3]Department of Applied Physics, California Institute of Technology, Pasadena, California 91125, USA

(Received 11 February 2013; published 31 May 2013)

We demonstrate optomechanically mediated electromagnetically induced transparency and wavelength conversion in silicon nitride (Si_3N_4) microdisk resonators. Fabricated devices support whispering gallery optical modes with a quality factor (Q) of 10^6, and radial breathing mechanical modes with a $Q = 10^4$ and a resonance frequency of 625 MHz, so that the system is in the resolved sideband regime. Placing a strong optical control field on the red (blue) detuned sideband of the optical mode produces coherent interference with a resonant probe beam, inducing a transparency (absorption) window for the probe. This is observed for multiple optical modes of the device, all of which couple to the same mechanical mode, and which can be widely separated in wavelength due to the large band gap of Si_3N_4. These properties are exploited to demonstrate frequency up-conversion and down-conversion of optical signals between the 1300 and 980 nm bands with a frequency span of 69.4 THz.

DOI: 10.1103/PhysRevLett.110.223603 PACS numbers: 42.50.Wk, 42.50.Ct, 85.85.+j

Recent demonstrations of strong radiation pressure interactions in cavity optomechanics have focused on the resolved sideband regime, where mechanical sidebands of the optical mode lie outside its linewidth [1]. Such systems have been used in laser cooling a mechanical oscillator to its ground state [2,3], coherent interference effects such as electromagnetically induced transparency (EIT) [4,5], parametrically driven normal mode splitting [6–8], and observing energy exchange between the optical and mechanical systems [8,9]. Here, we study a system consisting of a small diameter silicon nitride (Si_3N_4) microdisk in which multiple high quality factor optical modes couple to a 625 MHz mechanical radial breathing mode. We demonstrate optomechanically mediated EIT and wavelength conversion [10–13], up- and down-converting signals across the widely separated 1300 and 980 nm wavelengths bands. Our results establish Si_3N_4 as a viable platform for chip-scale cavity optomechanics in the resolved sideband regime. More generally, Si_3N_4 offers potential integration of cavity optomechanics with numerous classical and quantum photonic elements, including ultra-low-loss passive components [14], microcavity frequency combs [15] and spectrally narrow mode-locked lasers [16], and integrated superconducting single photon detectors [17].

In the context of chip-scale guided wave devices, experiments making use of frequency-resolved mechanical sidebands have largely been in two systems exhibiting significantly different parameter regimes: silica microtoroid cavities [4,8] and silicon photonic and phononic crystal resonators (optomechanical crystals) [3,5,18]. Silica microtoroids support ultrahigh quality factor optical modes ($Q_o > 10^7$, decay rate $\kappa/2\pi \approx 10$ MHz) that are coupled to $\gtrsim 50$ MHz frequency mechanical modes with a zero-point optomechanical coupling rate $g_0/2\pi \gtrsim 1$ kHz. In contrast, silicon optomechanical crystals have $Q_o \approx 10^6$ ($\kappa/2\pi \gtrsim 200$ MHz) modes that couple to few GHz mechanical modes with $g_0/2\pi \approx 1$ MHz. Though similar physics has been studied in both, there are qualitative benefits in each system. Higher mechanical frequencies yield lower phonon occupation numbers for a given temperature and larger bandwidths (for a given mechanical quality factor Q_m) in phenomena like slow light [5] and wavelength conversion [12]. Wide band gap materials like silica enable operation across a broad wavelength range, including visible wavelengths common to atomic systems, and are free of nonlinear loss mechanisms at most wavelengths. Here, we develop Si_3N_4 microdisks as a chip-scale cavity optomechanical platform that combines many advantageous features of the aforementioned systems. This includes near-GHz mechanical frequencies, a high frequency-Q_m product (6×10^{12} Hz), a straightforward optical mode structure with multiple high-Q_o ($\approx 10^6$) optical modes coupled to the same mechanical mode ($g_0/2\pi \approx 8$ kHz), a wide band gap with broad optical transparency, and low nonlinear loss. Although microdisk optomechanical devices have been used in sensitive optical transduction of motion [19] (including at GHz frequencies [20]), mechanical oscillation and cooling [21], and optical mode tuning [22], we note the qualitative difference with respect to our experiments, which demonstrate coherent interference phenomena like EIT and wavelength conversion.

Microdisk cavities [Fig. 1(a)] are fabricated in 350 nm thick Si_3N_4-on-silicon, as described in the Supplemental Material [23]. The choice of geometry is informed by finite element simulations [23]. The disk diameter (10 μm) is small enough to support a high frequency (> 0.6 GHz)

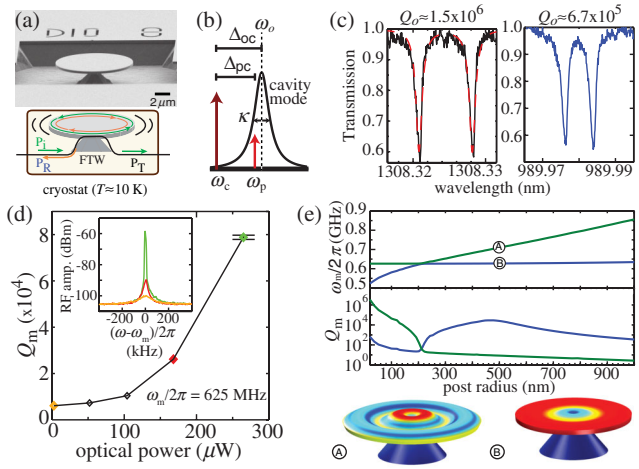

FIG. 1 (color online). (a) Scanning electron micrograph and schematic of the FTW coupling to the disk, with optical (green and orange arrows) and mechanical (black curved lines) modes depicted. (b) Sideband spectroscopy: $\omega_{o,c,p}$ are the frequencies of the optical cavity mode, control field, and probe field, respectively, and κ is the cavity mode linewidth. (c) Room-temperature 1300 and 980 nm band optical modes. (d) Room-temperature mechanical Q as a function of input optical power (laser blue detuned from the optical mode) for the radial breathing mode. The inset shows the mechanical mode spectrum at three highlighted optical powers. (e) Finite-element-method calculated frequency (top) and mechanical Q (middle) for two modes labeled Ⓐ and Ⓑ, as a function of top pedestal radius. The modes anticross at a radius of 200 nm. (bottom) Displacement profiles for a radius of 500 nm.

mechanical radial breathing mode and large enough to avoid intrinsic optical radiation loss. The top pedestal diameter (200 nm) limits coupling between the radial breathing mode and lossy mechanical modes of the supporting pedestal [Fig. 1(e)]. Basic optical and mechanical properties are experimentally characterized using swept-wavelength spectroscopy, with light coupled into the devices using an optical fiber taper waveguide (FTW). At room temperature and under moderate vacuum (0.002 Pa $\approx 2 \times 10^{-5}$ torr), an optical quality factor Q_o as high as 2×10^6 at both 1300 and 980 nm is measured. Figure 1(c) shows representative scans for a device whose total Q_o is 1.5×10^6 at 1308 nm, and 6.7×10^5 at 990 nm (the intrinsic Q_o based on the depth of coupling is 1.7×10^6 and 7.6×10^5, respectively). Mechanical modes are measured by tuning the laser to the shoulder of an optical mode and detecting optical field fluctuations induced by the thermally driven motion of the disk. We observe the fundamental radial breathing mode at $\omega_m/2\pi \approx 625$ MHz, with undriven Q_m of 6×10^3 [Fig. 1(d)]. To improve thermal stability, the device is cooled in a liquid He cryostat to ≈ 10 K. We see an increase in the undriven Q_m to 1×10^4, yielding a frequency-Q_m product of 6×10^{12} Hz, which approaches the recently demonstrated value of 2×10^{13} Hz in Si_3N_4 (albeit at a much lower frequency of 10 MHz [24]). Cryogenic operation also tends to degrade Q_o (by as much as a factor of 3), which we attribute to cryogettering of material on the sample. The splitting in the doublet mode optical transmission spectra, which results from backscattering [25], also changes. These changes vary from cooldown to cooldown.

In the context of cavity optomechanics, EIT is an increase in the transmission of a near-resonant probe beam (at frequency ω_p) through an optical cavity mode (at frequency ω_o) that results when a strong control field (at frequency ω_c) is red detuned by $\Delta_{oc} = \omega_o - \omega_c = \omega_m$ [Fig. 1(b)], so that anti-Stokes photons generated by scattering of the control field by the mechanical resonator interfere with the probe and create a transparency window for it [4,5,26]. We focus on the reflected signal from the cavity present in our microdisks due to the aforementioned backscattering, and for which EIT results in a narrow dip in the reflection peak. Our measurement setup is described in detail in the Supplemental Material [23].

We first study the system in the 1300 nm band by sweeping $\Delta_{pc} = \omega_p - \omega_c$ at different values of Δ_{oc}. For each Δ_{oc}, we take two sweeps of Δ_{pc}, one over a broad range to trace the overall cavity reflection spectrum and lock the control laser, and the other over a narrow range to resolve the narrow EIT dip [23]. A series of spectra is shown in Fig. 2(a), where Q_o has slightly degraded compared to its room-temperature value, with $\kappa/2\pi \approx 180$ MHz. As observed in previous work [4,5], the EIT dip always appears at $\Delta_{pc} = \omega_m$, and its width is given by the total mechanical damping rate γ, which is the sum of the intrinsic rate γ_m and the optomechanically induced damping rate $\gamma_{OM} = C\gamma_m$, where C is the cooperativity parameter. $C = (4G^2/\kappa\gamma_m)$, where $G = g_0\sqrt{N}$ is the parametrically enhanced coupling rate provided by N intracavity control field photons. We reach $C \approx 0.45$ by increasing the optical power before the system is thermally unstable.

To more quantitatively understand the EIT effect and assess the zero-point optomechanical coupling rate g_0, we set $\Delta_{oc} \approx \omega_m$ and measure the normalized reflection spectrum as a function of control field power [Fig. 2(b)]. For this set of measurements, Q_o degraded upon cooldown to $\kappa/2\pi \approx 550$ MHz [inset to Fig. 2(c)], while the mechanical mode had $\gamma_m/2\pi \approx 63$ kHz. We fit each normalized reflection spectrum using the theory presented in Ref. [5], where the amplitude reflection coefficient $r(\Delta_{pc})$ normalized to unity is given as

$$r(\Delta_{pc}) = -\frac{1}{1 + \frac{2i(\Delta_{oc} - \Delta_{pc})}{\kappa} + \frac{C}{\frac{2i(\omega_m - \Delta_{pc})}{\gamma_m} + 1}}. \quad (1)$$

$R(\Delta_{pc}) = |r|^2$ is the normalized reflected intensity, and the contrast in the EIT dip $\Delta R = 1 - R(\Delta_{pc} = \omega_m)$ is plotted as a function of control field power in Fig. 2(c) [in the limit $\Delta_{oc} = \omega_m$, $\Delta R = 1 - 1/(1 + C)^2$]. Recalling

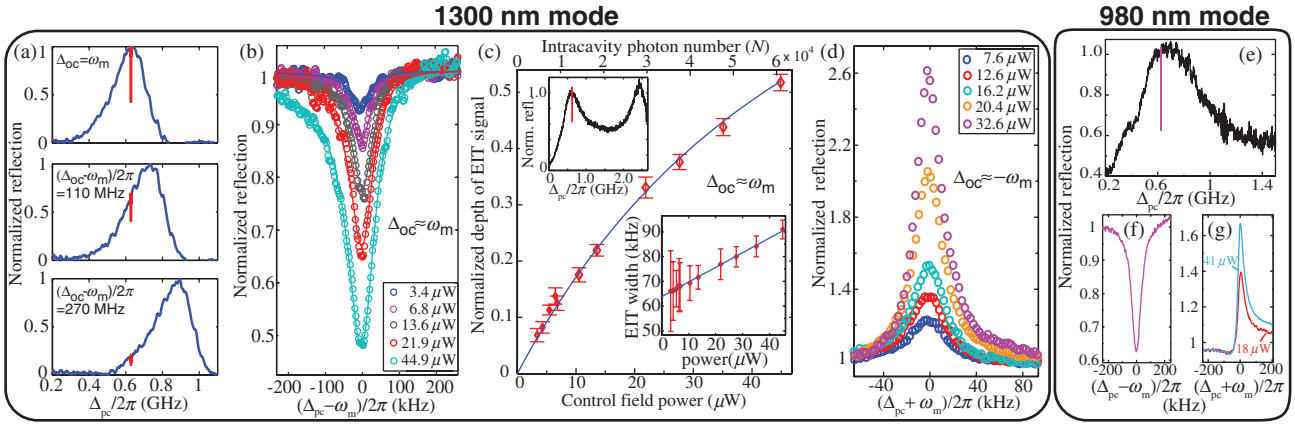

FIG. 2 (color online). EIT/EIA measurements for a (a)–(d) 1300 nm and (e)–(g) 980 nm mode. (a) Reflection spectra with the optical mode-control field detuning (Δ_{oc}) stepped and the probe-control detuning (Δ_{pc}) swept. Blue (red) curves are taken over a broad (narrow) range of Δ_{pc}. (b) Zoomed-in reflection spectra around the EIT dip (open circles are data, solid lines are fits) and (c) depth of the EIT dip as a function of control field power, for $\Delta_{oc} \approx \omega_m$. The upper inset shows the broad reflection spectrum corresponding to the data in (b),(c), for which Q_o had degraded with respect to that in (a). The lower inset shows the width of the EIT dip in (b) as a function of control field power. (d) Zoomed-in reflection spectra for $\Delta_{oc} = -\omega_m$, for which EIA is observed. (e) Broad and (f), (g) narrow reflection spectra as a function of Δ_{pc} for a cavity mode in the 980 nm band. In (e),(f), $\Delta_{oc} \approx \omega_m$, while in (g), $\Delta_{oc} \approx -\omega_m$.

that $C = (4Ng_0^2/\kappa\gamma_m)$, we use Eq. (1) in a fit to extract $g_0/2\pi \approx 7.8$ kHz, where knowledge of the FTW loss, cavity mode spectrum, and Δ_{oc} allows us to estimate N at each pump power [23]. We see good agreement between experiment and theory, further supported by the linear increase in the EIT dip width with pump power [lower inset to Fig. 2(c)]. However, the experimentally determined g_0 is nearly two times smaller than that predicted from finite element simulations ($g_0/2\pi \approx 15$ kHz) that exclusively consider the contribution due to moving dielectric boundaries. A study of whether photoelastic effects may play a role [27] in this discrepancy is under way. Finally, shifting the control field to the blue detuned side of the optical mode ($\Delta_{oc} \approx -\omega_m$) results in electromagnetically induced absorption (EIA) evidenced by a peak in the center of the reflection spectrum that increases with optical power [Fig. 2(d)].

Whispering gallery mode cavities can support high-Q optical modes over a broad range of wavelengths. As a result, multiple, broadly spaced optical modes may be expected to couple to the same mechanical mode, which we observe in our measurements. Figures 2(e)–2(g) present EIT and EIA data for a 980 nm band optical mode ($\kappa/2\pi \approx 750$ MHz) that couples to the 625 MHz radial breathing mode. We observe similar behavior as seen for the 1300 nm band mode, though the maximum contrast of the EIT dip and EIA peak are a little smaller, likely due to lower Q_o which is not fully compensated by higher optical power before thermal instability sets in.

One application of multiple optical modes coupled to the same mechanical mode is in wavelength conversion, as outlined in theory [11] and recently demonstrated in silicon optomechanical crystals [12] and silica microspheres [13]. The application of two control pumps, each red detuned from a corresponding optical mode by ω_m, opens up a pair of transparency windows over which wavelength conversion mediated by the mechanical resonator can occur [Figs. 3(a) and 3(b)]. Input signals over a bandwidth set by the damped mechanical resonator can be up-converted or down-converted, with an internal conversion efficiency that depends on the cooperativity achieved for each optical mode.

We proceed following the recent experiments of Hill *et al.* [12], with a simplified experimental setup shown in Fig. 3(a) and described further in the Supplemental Material [23]. We first alternate between EIT spectroscopy in the 1300 and 980 nm bands. These measurements are done to ascertain Δ_{oc} for each mode, as well as the cooperativity achieved. For the experiments that follow, $\Delta_{oc} \approx \omega_m$ for both control pumps. Focusing first on frequency up-conversion, we amplitude modulate the 1300 nm laser to generate an input probe signal that is detuned from the control pump by Δ_{pc}. The control pump and input probe signal in the 1300 nm band are combined with the control pump in the 980 nm band and sent into the FTW-coupled microdisk. Light exiting the device is then spectrally separated into the 980 and 1300 nm bands. As the converted tone in the 980 nm band is detuned with respect to the 980 nm band control pump by Δ_{pc}, the beating of the two fields is recorded on an electronic spectrum analyzer after photodetection. The input probe-control field detuning Δ_{pc} is then swept to assess the conversion bandwidth [Fig. 3(b)].

The Supplemental Material [23] shows the optical transmission spectrum measured for modes in the 1300 and 980 nm bands. The top of Fig. 3(c) shows a series of measurements for frequency up-conversion, in which the power in the 1285 nm control pump is held fixed at its maximum value, and the power in the 990 nm control

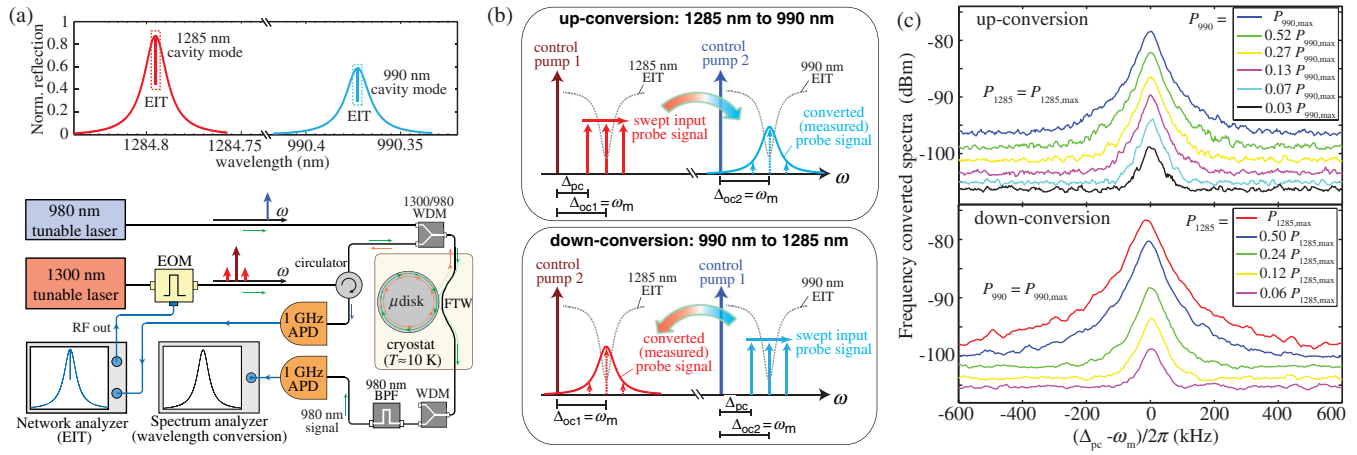

FIG. 3 (color online). Wideband wavelength conversion: (a), (b) Schematics of the process. (a) Top: Frequency conversion occurs over a pair of transparency windows opened up in two of the cavity's optical modes through EIT. Bottom: Experimental setup for up-conversion. The frequency converted signal transmitted past the cavity is measured on a rf spectrum analyzer. (b) Zoomed-in schematics of the EIT transparency windows in (a). Top: In frequency up-conversion, a 1285 nm control pump and 990 nm control pump are used to convert a 1285 nm input probe signal to 990 nm. The detuning between the 1285 nm input probe signal and control pump can be swept over a range given by the bandwidth of the damped mechanical oscillator. (Bottom) In frequency down-conversion, the input probe signal is at 990 nm, and the control pumps mediate conversion to 1285 nm. (c) Up-converted (top) and down-converted (bottom) signals measured as the relevant input probe signal-control pump detuning (Δ_{pc}) is swept. In up-conversion (down-conversion), the 1285 nm (990 nm) control pump power is fixed at $P_{1285,\mathrm{max}} = 63.8\ \mu$W ($P_{990,\mathrm{max}} = 9.0\ \mu$W) and the 990 nm (1285 nm) control pump power is stepped.

pump is stepped. Each displayed trace taken at fixed control pump powers represents the envelope of a series of frequency converted spectra measured on the rf spectrum analyzer, in which the frequency separation between the input probe signal and adjacent control pump Δ_{pc} is swept. This provides us with an estimate of the bandwidth of the conversion process, which matches that of the damped mechanical oscillator. As the power is increased towards its highest values, the conversion efficiency (the photon number ratio of the converted signal to input signal) begins to saturate, with internal (external) conversion efficiencies reaching $\approx 16.1\%$ (0.49%) [23].

The maximum expected internal conversion efficiency is estimated from the cooperativities of the two modes, C_1 and C_2 [12,13], as $\eta = 4C_1C_2/(1 + C_1 + C_2)^2$. While in Fig. 2, $C_1 = C_2 = 0.45$ was reached, corresponding to a maximum $\eta = 22\%$, the lower Q_os measured here caused a reduction in C_1 and C_2 that was not fully compensated by additional optical power, thus explaining the lower efficiency. The external conversion efficiency of 0.49% is given by the product of the internal efficiency and the waveguide-cavity incoupling and outcoupling efficiencies, which are 29.2% and 10.3%, respectively.

For frequency down-conversion, the roles of the 990 and 1285 nm lasers are reversed [Fig. 3(b)], as now an input probe signal at 990 nm is combined with control pumps in the 980 and 1300 nm bands to generate converted tones in the 1300 nm band. The resulting down-conversion data measured on the rf spectrum analyzer are shown in the bottom of Fig. 3(c). The data are taken by fixing the power in the 990 nm control pump at its maximum value and stepping the power in the 1285 nm control pump. Each trace is the envelope of a series of frequency converted spectra, where the detuning between input probe signal and adjacent control pump Δ_{pc} is swept.

Eventually, such wavelength conversion could connect quantum optical technology at wavelengths below 1000 nm (e.g., quantum memories) and at 1300 nm (low loss and dispersion optical fibers). Several improvements must be made for such quantum frequency conversion [28] to be feasible. Higher cooperativities and more efficient waveguide-cavity coupling are needed to improve the conversion efficiency. Reduced mechanical damping is one key to increased cooperativity. As simulations [Fig. 1(e)] indicate that coupling to pedestal modes may limit Q_m, smaller pedestal diameters or isolation of the disk periphery from a central, pedestal-supported region [29] may provide improvement.

The generation of noise photons is a crucial consideration for applications such as frequency conversion of single photon states [30], and has contributions that stem from the limited sideband resolution of the system (e.g., Stokes scattered photons) and the thermal occupancy of the mechanical resonator ($\langle n\rangle_{\mathrm{th}} \approx 330$ for the mechanical mode at 10 K; laser cooling in our experiments reduces this by at most $\approx 33\%$). In contrast, recent work in optomechanical crystals [12] cooled the system close to the ground state ($\langle n\rangle_{\mathrm{th}} \approx 3$), whereas experiments done at room temperature in microspheres [13] have an even larger noise contribution ($\langle n\rangle_{\mathrm{th}} \approx 4 \times 10^4$).

Finally, Si_3N_4 devices may benefit by supporting a large intracavity photon number N without nonlinear loss which, for example, influences Si optomechanical crystals at $N \gtrsim 300$ [3]. We reach $N \approx 6 \times 10^4$, and further increases are not limited by nonlinear loss but instead thermal stability. Techniques to lock Δ_{oc} beyond the relatively slow procedure we have adopted [23] would be of significant benefit. Finally, increased g_0 could dramatically improve performance, given the squared dependence of the cooperativity on this parameter. While large increases in g_0 are unlikely for microdisks, since significant decreases in diameter will result in radiation losses, recent designs of Si_3N_4 slot mode optomechanical crystals [31] suggest that such a system may be able to combine high frequency, large g_0, and large N.

Y. Liu and M. Davanço contributed equally to this work. We thank O. Painter for helpful discussions and loan of equipment. Y. L. acknowledges support under the NIST-ARRA Measurement Science and Engineering Fellowship Program Grant No. 70NANB10H026 through the University of Maryland. This work was partly supported by the DARPA/MTO MESO program.

*kartik.srinivasan@nist.gov

[1] T. J. Kippenberg and K. J. Vahala, Science **321**, 1172 (2008).
[2] J. D. Teufel, T. Donner, D. Li, J. W. Harlow, M. S. Allman, K. Cicak, A. J. Sirois, J. D. Whittaker, K. W. Lehnert, and R. W. Simmonds, Nature (London) **475**, 359 (2011).
[3] J. Chan, T. P. M. Alegre, A. H. Safavi-Naeini, J. T. Hill, A. Krause, S. Gröblacher, M. Aspelmeyer, and O. Painter, Nature (London) **478**, 89 (2011).
[4] S. Weis, R. Rivière, S. Deléglise, E. Gavartin, O. Arcizet, A. Schliesser, and T. J. Kippenberg, Science **330**, 1520 (2010).
[5] A. H. Safavi-Naeini, T. P. M. Alegre, J. Chan, M. Eichenfield, M. Winger, Q. Lin, J. T. Hill, D. E. Chang, and O. Painter, Nature (London) **472**, 69 (2011).
[6] S. Gröblacher, K. Hammerer, M. R. Vanner, and M. Aspelmeyer, Nature (London) **460**, 724 (2009).
[7] J. D. Teufel, D. Li, M. S. Allman, K. Cicak, A. J. Sirois, J. D. Whittaker, and R. W. Simmonds, Nature (London) **471**, 204 (2011).
[8] E. Verhagen, S. Deléglise, S. Weis, A. Schliesser, and T. J. Kippenberg, Nature (London) **482**, 63 (2012).
[9] V. Fiore, Y. Yang, M. C. Kuzyk, R. Barbour, L. Tian, and H. Wang, Phys. Rev. Lett. **107**, 133601 (2011).
[10] L. Tian and H. Wang, Phys. Rev. A **82**, 053806 (2010).
[11] A. H. Safavi-Naeini and O. Painter, New J. Phys. **13**, 013017 (2011); Y.-D. Wang and A. A. Clerk, Phys. Rev. Lett. **108**, 153603 (2012).
[12] J. T. Hill, A. H. Safavi-Naeini, J. Chan, and O. Painter, Nat. Commun. **3**, 1196 (2012).
[13] C. Dong, V. Fiore, M. Kuzyk, and H. Wang, Science **338**, 1609 (2012).
[14] J. F. Bauters, M. J. R. Heck, D. John, D. Dai, M.-C. Tien, J. S. Barton, A. Leinse, R. G. Heideman, D. J. Blumenthal, and J. E. Bowers, Opt. Express **19**, 3163 (2011).
[15] J. S. Levy, A. Gondarenko, M. A. Foster, A. C. Turner-Foster, A. L. Gaeta, and M. Lipson, Nat. Photonics **4**, 37 (2010).
[16] M. Peccianti, A. Pasquazi, Y. Park, B. E. Little, S. T. Chu, D. J. Moss, and R. Morandotti, Nat. Commun. **3**, 765 (2012).
[17] C. Schuck, W. H. P. Pernice, and H. X. Tang, Appl. Phys. Lett. **102**, 051101 (2013).
[18] M. Eichenfield, J. Chan, R. M. Camacho, K. J. Vahala, and O. Painter, Nature (London) **462**, 78 (2009).
[19] G. Anetsberger, O. Arcizet, Q. P. Unterreithmeier, R. Rivière, A. Schliesser, E. M. Weig, J. P. Kotthaus, and T. J. Kippenberg, Nat. Phys. **5**, 909 (2009); K. Srinivasan, H. Miao, M. T. Rakher, M. Davanço, and V. Aksyuk, Nano Lett. **11**, 791 (2011).
[20] L. Ding, C. Baker, P. Senellart, A. Lemaitre, S. Ducci, G. Leo, and I. Favero, Phys. Rev. Lett. **105**, 263903 (2010); X. Sun, K. Y. Fong, C. Xiong, W. H. P. Pernice, and H. X. Tang, Opt. Express **19**, 22 316 (2011).
[21] Q. Lin, J. Rosenberg, X. Jiang, K. J. Vahala, and O. Painter, Phys. Rev. Lett. **103**, 103601 (2009).
[22] G. S. Wiederhecker, L. Chen, A. Gondarenko, and M. Lipson, Nature (London) **462**, 633 (2009).
[23] See Supplemental Material at http://link.aps.org/supplemental/10.1103/PhysRevLett.110.223603 for details on simulations, fabrication, data fitting, experimental setups, and uncertainty estimates.
[24] D. J. Wilson, C. A. Regal, S. B. Papp, and H. J. Kimble, Phys. Rev. Lett. **103**, 207204 (2009).
[25] D. S. Weiss, V. Sandoghdar, J. Hare, V. Lefèvre-Seguin, J.-M. Raimond, and S. Haroche, Opt. Lett. **20**, 1835 (1995).
[26] G. S. Agarwal and S. Huang, Phys. Rev. A **81**, 041803 (2010).
[27] J. Chan, A. H. Safavi-Naeini, J. Hill, S. Meenehan, and O. Painter, Appl. Phys. Lett. **101**, 081115 (2012).
[28] P. Kumar, Opt. Lett. **15**, 1476 (1990).
[29] G. Anetsberger, R. Rivière, A. Schliesser, O. Arcizet, and T. J. Kippenberg, Nat. Photonics **2**, 627 (2008).
[30] M. Raymer and K. Srinivasan, Phys. Today **65**, No. 11, 32 (2012).
[31] M. Davanço, J. Chan, A. H. Safavi-Naeini, O. Painter, and K. Srinivasan, Opt. Express **20**, 24 394 (2012).